Electromechanical response of poly(vinylidenefluoride) thin films under acoustic stimuli

ARTICLE TEMPLATE

Electromechanical response of Poly(vinylidenefluoride) thin films under acoustic stimuli

Giuseppe Viola[a,b,‡], Jinke Chang[a,‡], Felix Steckler[a], Tadej Rojac[c], Nicholas Fantuzzi[d] and Wenhui Song[a]

[a]UCL Centre for Biomaterials in Surgical Reconstruction and Regeneration, Division of Surgery & Interventional Science, University College London, London NW3 2PF, United Kingdom
[b]School of Engineering and Material Science, Queen Mary University of London, 380 mile end Road, London E1 4NS, United Kingdom
[c]Electronic Ceramics Department, Jožef Stefan Institute, 1000 Ljubljana, Slovenia
[d]Department of Civil, Chemical, Environmental and Materials Engineering, University of Bologna, Viale del Risorgimento 2, 40136 Bologna, Italy

ARTICLE HISTORY
Compiled October 12, 2022

ABSTRACT
Understanding and controlling the vibration of piezoelectric components induced by oscillating external stimuli is essential to develop smart sensing and energy harvesting devices that convert mechanical energy into electricity. Piezoelectric polymers based on Poly(vinylidenefluoride) (PVDF) thin films are amongst the most widely studied materials for flexible sensors and harvesters. Despite the large amount of research on these materials, their electromechanical response under acoustic sound stimuli has not yet been studied in detail. In this work, a thorough investigation on the mechanical vibrations and electrical response of PVDF circular plates of different diameters in response to multiple sound wave frequencies (100Hz-10kHz) has been carried out to gain further understanding of the resonance behaviour and acousto-electric conversion mechanisms of vibrating PVDF thin films. The work is based on experimental data generated using an integrated piezo-acoustic laser vibrometry system and on a theoretical framework based on the continuum theory of thin plates. The developed model enables the prediction of the resonance frequencies in dependence of the plates' diameter, and suggests that the electrical voltage generated during vibrations is not solely originating from the piezoelectric properties of the films, but might be affected by additional factors, including the triboelectric effect. The results of this study are expected to have a strong impact on the investigation of piezoelectric vibrating plates and on the development of different types of transducers and energy harvesting devices.

KEYWORDS
piezoelectric plates; PVDF thin films; nonlinear vibrations; acoustic stimuli; resonance frequencies

CONTACT Nicholas Fantuzzi. Email: nicholas.fantuzzi@unibo.it
‡ These authors contributed equally to this work.

1. Introduction

Piezoelectric materials feature the reciprocal conversion of mechanical and electrical energy and are widely used as sensors, actuators, energy harvesting systems (Caliò et al. (2014); Toprak and Tigli (2014); Yadav et al. (2021)) and acoustic transducers, which convert acoustic waves into electrical signals via the direct piezoelectric effect (Jain et al. (2014); Liu et al. (2018)). The development of acoustic devices has started decades ago and significant improvements have been made ever since. Proctor (1982) proposed an improved piezoelectric acoustic emission transducer, while Gualtieri et al. (1994), and Safari and Akdogan (2008) have investigated several piezoelectric materials for acoustic-wave transducers. Studies on piezoelectric acoustic sensors have increased over the recent years (Ali and Prasad (2020)), providing smart solutions for various novel applications, including acoustic energy harvesting (Pillai and Deenadayalan (2014)), wireless communication (Drafts (2001)), wildlife monitoring (Baratchi et al. (2013)), surveillance (Kim et al. (2008)) and biomedical devices (Ahamed et al. (2018)). Harvesting of sound wave energy can be efficiently implemented in various places where acoustic energy abounds, such as factories, construction sites, roads, railways, airports and concert venues, and it can be safely harnessed to generate voltage (Pillai and Deenadayalan (2014); Choi et al. (2019)). Piezoacoustic systems with improved acoustic-electrical conversion are also being developed to improve the performance of miniaturized devices in communication technologies (Benech and Duchamp (2016); Hashimoto (2011); Roes et al. (2013)). In addition, the use of acoustic detectors is increasing in the ecology sector, with the purpose of monitoring wildlife activity that most often require highly sensitive piezoelectric devices to detect low sound levels (Baratchi et al. (2013); Mankin et al. (2011)). Other important applications of acoustic sensors are realized in surveillance, for the detection of undesired intrusions in protected places (Kim et al. (2008)). Acoustic-electric conversion is also suited in different types of acoustic biosensors (Fu et al. (2017)) and biomedical devices, such as cardiac pacemakers, implantable pressure sensors (Basaeri et al. (2016)) and artificial hearing aids for cochlea implants (Inaoka et al. (2011); Lee et al. (2014)).

In most acoustic and energy harvesting applications, the piezoelectric devices operate in resonance conditions, where maximum vibrations and large energy conversion are obtained (Erturk and Inman (2011); Kim et al. (2011); Liu et al. (2018)). The resonance frequencies can be tuned by modifying the mechanical properties of the vibrating components, as well as their geometry and mechanical and electrical boundary conditions. The identification and prediction of the resonance frequencies is crucial to validate the suitability of the devices for specific applications and to optimize their performance (Toprak and Tigli (2014); Caliò et al. (2014)). The use of piezoelectric polymers is particularly convenient in different applications where high flexibility, chemical stability and long-term reliability are required (Shin et al. (2018)). Due to their large compliance, piezoelectric polymers provide high sensitivity to external mechanical stimuli. Such structures have been extensively analyzed using numerical approaches for both static and dynamic regimes by Chanda and Sahoo (2021); Vieira and Araújo (2021); Cinefra et al. (2015a).

Piezoelectric polymers are typically used in thin film geometries, with poly(vinylidene fluoride) (PVDF) and its copolymer polyvinyledene difluoride–trifluoroethylene P(VDF-TrFE), being the most widely used materials (Eisenmenger and Haardt (1982); M. Ericka et al. (2005); Chen et al. (2017)). It worth to mention the work performed by Kong et al. (2021) who analyzed the fracture damage and friction mechanical properties of silicon dioxide/polyvinylidene composites.

Despite the intensive research carried out on PVDF-based materials over the last few decades, their response to acoustic waves and the resonance patterns have not been fully characterized. Previous studies have focused on the vibration of stretched PVDF ribbons fully clamped at their extremes (Mahidhar et al. (2013)), PVDF rectangular membranes fully clamped along the border (Sanz-Robinson et al. (2016); Wang et al. (2015)), PVDF trapezoidal slits fully constrained along the entire perimeter (Shintaku et al. (2010)), and circular membranes made up of PVDF and PVDF-TrFE nanofibers (Lang et al. (2016); Viola et al. (2020)). The present study reports a thorough experimental investigation of the mechanical and electrical response of PVDF piezoelectric thin films to acoustic stimuli, with particular focus on the dependence of the resonance frequency on the size of circular plates. A theoretical framework that describes the experimental results with high accuracy has been developed, founding the basis for the mathematical description of similar phenomena in other piezoelectric systems. The results provide useful insights into the development of energy harvesting and piezoacoustic systems. Moreover, they will support our ongoing research activities focused on the engineering of novel biocompatible materials for cochlear replacement, and can be regarded as a solid ground for the optimization of more sophisticated acoustic sensing systems currently under development.

2. Experimental details

Commercial poled films of PVDF (110μm thickness) were purchased from Precision Acoustics Ltd (UK). The films were clamped between two plates containing holes with different diameter (10, 16, 20, 30 mm), fabricated with a 3D printing machine (Makerbot V2, US), using poly(lactic acid) filaments (see blue clamps in Figure 1a). The purpose of the different-sized holes was to study the effects of geometry on the resonance frequency of the vibrating films. To acquire the electrical voltage generated during vibration, conductive copper stripes were placed on the area surrounding each hole. The vibrations of these films induced by acoustic sound were experimentally studied using a Doppler vibrometer device, equipped with a laser pointer (MSA-050 Microsystem Analyzer, by Polytech, Germany) and a mouth simulator capable of generating acoustic waves of different intensity (80-120 dB) in the range 0.1-20kHz frequency (Type 4227-A, Brüel & Kjaer, Denmark). To measure the voltage output, voltage buffers were used due to the high impedance of the tested devices, which were connected to a data acquisition device (DAQ) (Powerlab 16, ADInstruments), to synchronize the acoustic signal generated by the mouth simulator with the displacement and voltage signals. The plates were sandwiched between two purposely-made clamps, which allowed holding the films at a distance of approximately 6 cm above the mouth simulator (see Figure 1b). The laser pointer was focused on the centre of each circular films, whose displacement was measured via the Doppler effect.

Acoustic sine waves with a linearly decreasing frequency from 10 kHz to 100Hz (as shown in Fig. 2) were generated by the mouth simulator (see Fig.1b) over a time period of two minutes (rate change of approximately 82.5 Hz/s), during which the displacement and the voltage output signals were simultaneously recorded. The tests were carried out using waves with a sound pressure level (SPL) of 84 dB (as measured by a probe placed closed to the bottom side of the films), which presented variations of approximately $\pm$15 dB during the frequency sweep. Thus, the exciting force (see Figure 2) is an approximately regular wave at 84 dB ($\approx$ 0.317 Pa) with a variable

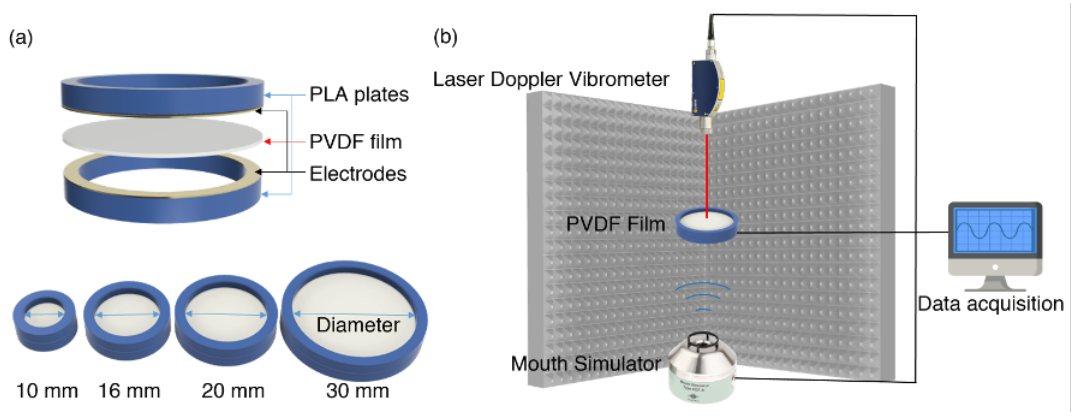

Figure 1. Schematics of the samples tested (a) and of the laser vibrometer device (b).

frequency according to the function:

$$\omega = 2\pi(-82.454t + 10030), \quad \text{for} \quad 0 \text{ s} < t < 120 \text{ s} \tag{1}$$

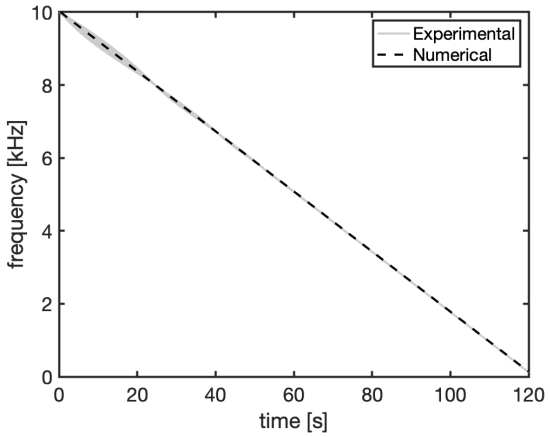

Figure 2. Time-variation of the sound wave frequency during the experimental and numerical tests.

3. Theoretical formulation

The vibrations of piezoelectric plates have been extensively studied in the literature (Carrera et al. (2008); Paul and Natarajan (1994); Zhao et al. (2020); Liu et al. (2011); Zhou (2021)). Several researchers gave proof that analytical and numerical techniques can be used in treating the problem of piezoelectric plates (Cinefra et al. (2015b); Tocci Monaco et al. (2021a,b)). Among all, Hosseini-Hashemi et al. (2010); Hosseini Hashemi et al. (2010) proposed a 3-D solutions for circular/annular plates integrated with piezoelectric layers, and Zhang et al. (2006) presented a 3-D vibration analysis of multilayered piezoelectric composite plates.

In this study, the theory of isotropic plates is initially considered to solve the mechanical vibration problem. The piezoelectric effect due to the deformation is given as

a consequence of the coupling at the constitutive level rather than from the solution of the system of equations. This can be shown by displaying the constitutive equations of piezoelectric materials where the coupling between elastic and electric effects is clearly visible (Tiersten (2013)). The resultant equilibrium equations are simply a consequence of such coupling; therefore, the elastic problem is firstly solved and the piezoelectric effect is computed afterwards (Duan et al. (2005); Mo et al. (2014)). For the development of the equation of motions of PVDF plates, the simplified method already presented by Mo et al. (2014) has been considered and summarized below for the present specific problem.

A circular PVDF plate is taken clamped at the outer edge. The plate of radius R and thickness h_p are described in cylindrical coordinates (r, θ, z).

3.1. *Equation of motion*

In the experimental tests, only the vibrations of the central point of the plate have been monitored; hence, the present problem is studied in axis-symmetric conditions. Moreover, due to the small thickness-to-width ratios considered in the present case, the classical thin plate theory has been applied. In this context, the displacement field of the plate in cylindrical coordinates can be represented by:

$$\begin{aligned} u_r(r,z,t) &= u(r,t) - z\frac{\partial w}{\partial r} \\ u_z(r,z,t) &= w(r,t) \end{aligned} \tag{2}$$

Where u_r and u_z are the in-plane and out-of-plane displacements of the plate, and u, w are the kinematic parameters, which identify in-plane and out-of-plane motion. For the present Kirchhoff theory, the rotation is modelled as the derivative of the transverse motion leading to no shear deformation, which is a suitable assumption, due to the small thickness-to-radius ratio (lower than 1/50) of the films studied. The term r is the radial coordinate and t indicates time, so that the strains with the von-Kármán nonlinear terms take the form:

$$\begin{aligned} \varepsilon_r &= \frac{\partial u}{\partial r} + \frac{1}{2}\left(\frac{\partial w}{\partial r}\right)^2 - z\frac{\partial^2 w}{\partial r^2} = \varepsilon_r^{(0)} + z\varepsilon_r^{(1)} \\ \varepsilon_\theta &= \frac{u_r}{r} = \frac{u}{r} - \frac{z}{r}\frac{\partial w}{\partial r} = \varepsilon_\theta^{(0)} + z\varepsilon_\theta^{(1)} \end{aligned} \tag{3}$$

The other deformations are identically zero due to the Kirchhoff's assumptions and axis-symmetric conditions.

If one initially neglects the piezoelectric properties, as mentioned above, the plate can be treated as isotropic. The constitutive equations for isotropic circular plates can be written as:

$$\begin{Bmatrix} \sigma_r \\ \sigma_\theta \end{Bmatrix} = \frac{1}{S_{31}(1-\nu_p^2)} \begin{bmatrix} 1 & \nu_p \\ \nu_p & 1 \end{bmatrix} \begin{Bmatrix} \varepsilon_r \\ \varepsilon_\theta \end{Bmatrix} \tag{4}$$

where $S_{31} = 1/E_p$, which represents the in-plane elastic compliance and E_p the elastic modulus of the plate. Since the piezoelectric coupling is initially neglected, the strain

energy of the plate is given by:

$$
\begin{aligned}
U &= \pi \int_0^R \int_{-h/2}^{h/2} (\sigma_r \varepsilon_r + \sigma_\theta \varepsilon_\theta) r \; dz \; dr \\
&= \pi \int_0^R \int_{-h/2}^{h/2} \frac{1}{S_{31}(1-\nu_p^2)} (\varepsilon_r^2 + \varepsilon_\theta^2 + 2\nu_p \varepsilon_r \varepsilon_\theta) r \; dz \; dr \\
&= \pi \int_0^R \int_{-h/2}^{h/2} \frac{1}{S_{31}(1-\nu_p^2)} ((\varepsilon_r^{(0)} + z\varepsilon_r^{(1)})^2 + (\varepsilon_\theta^{(0)} + z\varepsilon_\theta^{(1)})^2 + 2\nu_p(\varepsilon_r^{(0)} + z\varepsilon_r^{(1)})(\varepsilon_\theta^{(0)} + z\varepsilon_\theta^{(1)})) r \; dz \; dr \\
&= \pi D_s \int_0^R \left((\varepsilon_r^{(0)})^2 + (\varepsilon_\theta^{(0)})^2 + 2\nu_p \varepsilon_r^{(0)} \varepsilon_\theta^{(0)} \right) r \; dr + \pi D_b \int_0^R \left((\varepsilon_r^{(1)})^2 + (\varepsilon_\theta^{(1)})^2 + 2\nu_p \varepsilon_r^{(1)} \varepsilon_\theta^{(1)} \right) r \; dr \\
&= U_s + U_b
\end{aligned}
\tag{5}
$$

where the stretching stiffness is $D_s = h_p(S_{31}(1-\nu_p^2))^{-1}$ and the bending stiffness is $D_b = h_p^3/(12(1-\nu_p^2))$. From Eq. (5), the stretching U_s and bending U_b contributions to the total strain energy can be clearly identified.

The strain energy due to stretching can be written in terms of the displacements as:

$$
U_s = \pi D_s \int_0^R \left[\left(\frac{\partial u}{\partial r} \right)^2 + \left(\frac{\partial w}{\partial r} \right)^2 \left(\frac{\partial u}{\partial r} + \frac{1}{4} \left(\frac{\partial w}{\partial r} \right)^2 \right) + \frac{u}{r} \left(\frac{u}{r} + 2\nu_p \left(\frac{\partial u}{\partial r} + \frac{1}{2} \left(\frac{\partial w}{\partial r} \right)^2 \right) \right) \right] r \; dr \tag{6}
$$

It is assumed that the mode of vibration of the plate follows the one of the quasi-static deformation under uniform pressure; thus, the displacements field can be expressed as Mo et al. (2014):

$$
w = w_0 \left(1 - \left(\frac{r}{R} \right)^2 \right)^2, \quad u = r(R-r)(c_1 + c_2 r) \tag{7}
$$

where w_0 is the lumped maximum plate deflection at the plate center ($r = 0$) and c_1 and c_2 are two coefficients that take the form (due to equilibrium condition, Mo et al. (2014))

$$
c_1 = \frac{1}{126} \frac{w_0^2 \, (179 - 89\nu_p)}{R^3}, \quad c_2 = \; -\frac{1}{42} \frac{w_0^2 \, (79 - 13\nu_p)}{R^4} \tag{8}
$$

so that u becomes:

$$
u = \frac{w_0^2}{126} \frac{r}{R^2} \left(1 - \frac{r}{R} \right) \left(179 - 89\nu_p - 3(79 - 13\nu_p) \frac{r}{R} \right) \tag{9}
$$

The bending strain energy takes the form:

$$
U_b = \pi D_b \int_0^R \left[\left(\frac{\partial^2 w}{\partial r^2} \right)^2 + \frac{1}{r^2} \left(\frac{\partial w}{\partial r} \right)^2 + \frac{2\nu_p}{r} \frac{\partial w}{\partial r} \frac{\partial^2 w}{\partial r^2} \right] r \; dr \tag{10}
$$

The total strain energy is given by the sum of the two energy contributions $U = U_s + U_b$, which leads to the following expression:

$$U = \frac{\pi h_p w_0^2}{39690 R^2 S_{31}(1-\nu_p^2)} \left[w_0^2 \left(-2791\nu_p^2 + 4250\nu_p + 7505 \right) + 35280 h_p^2 \right] \tag{11}$$

Eq. (11) reports both linear and nonlinear terms. In particular, for a fixed material (e.g. S_{31} and ν_p unchanged) the linear part of the strain energy changes with the cubic of the plate thickness, whereas its nonlinear part changes linearly.

Since a sinusoidal time-history $p(r,t) = p_0 e^{i\omega t}$ is considered, the potential energy V_E (equal to the external work W_E with negative sign) for such loads can be written as:

$$V_E = -W_E = -2\pi \int_0^R p(r,t) w r \, dr = -\frac{1}{3}\pi p_0 w_0 R^2 \tag{12}$$

The kinetic energy takes the form:

$$K = \rho\pi \int_0^R \left[h_p \dot{u}^2 + h_p \dot{w}^2 + \frac{h_p^3}{12} \left(\frac{\partial \dot{w}}{\partial r} \right)^2 \right] r dr \tag{13}$$

Note that the kinetic energy includes bulk and rotary inertia terms. The former becomes larger than the latter when considering thin plates. However, both components are considered here to include the effect of rotary inertia in the following computations. By performing the integrations, the kinetic energy becomes:

$$K = \frac{\pi \rho h_p}{2} \left[\frac{\left(62963\nu_p^2 - 89314\nu_p + 50651 \right) \dot{w}_0^4}{6667920} + \left(\frac{R^2}{5} + \frac{h_p^2}{9} \right) \dot{w}_0^2 \right] \tag{14}$$

According to the Hamilton's principle, the dynamic equilibrium verifies the condition:

$$\int_{t_1}^{t_2} \Big(\delta U + \delta V_E - \delta K \Big) dt = \int_{t_1}^{t_2} \left[\left(\frac{\partial U}{\partial w_0} + \frac{\partial V_E}{\partial w_0} \right) \delta w_0 - \frac{\partial K}{\partial \dot{w}_0} \delta \dot{w}_0 \right] dt = 0 \tag{15}$$

where t_1 and t_2 indicate two generic time instants. The derivative terms in Eq.(15) take the form:

$$\frac{\partial U}{\partial w_0} = \frac{2\pi h_p}{19845 R^2 S_{31}(1-\nu_p^2)} \left(\left(-2791\nu_p^2 + 4250\nu_p + 7505 \right) w_0^3 + 17640 h_p^2 w_0 \right) \tag{16}$$

$$\frac{\partial V_E}{\partial w_0} = -\frac{\pi p_0 R^2}{3} \tag{17}$$

$$\frac{\partial K}{\partial \dot{w}_0} = \pi \rho h_p \left[\frac{\left(62963\nu_p^2 - 89314\nu_p + 50651 \right) \dot{w}_0^3}{3333960} + \left(\frac{R^2}{5} + \frac{h_p^2}{9} \right) \dot{w}_0 \right] \tag{18}$$

Integration by parts with respect to time allows the equation of motion to be obtained. The final form of the nonlinear dynamic equilibrium equation reads:

$$\begin{aligned} 0 =& \frac{2h_p}{19845R^2S_{31}(1-\nu_p^2)}\left[\left(-2791\nu_p^2+4250\nu_p+7505\right)w_0^3+17640h_p^2w_0\right] \\ & -\frac{R^2}{3}p_0+\rho h_p\left[\frac{\left(62963\nu_p^2-89314\nu_p+50651\right)}{3333960}\ddot{w}_0^3+\left(\frac{R^2}{5}+\frac{h_p^2}{9}\right)\ddot{w}_0\right] \end{aligned} \tag{19}$$

From the equation above, the following compact form can be easily obtained:

$$m_3\ddot{w}_0^3+m_1\ddot{w}_0+k_1w_0+k_3w_0^3=f_1 \tag{20}$$

where

$$m_3=\rho h_p\frac{\left(62963\nu_p^2-89314\nu_p+50651\right)}{3333960},\quad m_1=\frac{\rho h_pR^2}{9}\left(\frac{9}{5}+\frac{h_p^2}{R^2}\right) \tag{21}$$

$$k_3=\frac{2h_p}{19845R^2S_{31}(1-\nu_p^2)}\left(-2791\nu_p^2+4250\nu_p+7505\right),\quad k_1=\frac{16h_p^3}{9R^2S_{31}(1-\nu_p^2)} \tag{22}$$

$$f_1=\frac{R^2}{3}p_0 \tag{23}$$

where subscripts $_1$ and $_3$ indicate linear and nonlinear terms, respectively. Equation (20) is the equivalent single-degree of freedom equation of motion of the present PVDF circular plate for nonlinear forced vibrations. It is remarked that both stiffness and mass include a nonlinear term.

The linear mass m_1 is quadratic with the plate radius, whereas the nonlinear component m_3 is constant. On the other hand, both linear k_1 and nonlinear k_3 stiffnesses are quadratic with the radius. Thus, by computing the ratio between nonlinear and linear quantities for mass and stiffness, the following relationships can be obtained:

$$\frac{m_3}{m_1}=\frac{62963\nu_p^2-89314\nu_p+50651}{74088(9R^2-5h_p^2)},\quad \frac{k_3}{k_1}=\frac{-2791\nu_p^2+4250\nu_p+7505}{17640} \tag{24}$$

Thus, in large plates, it is expected to have a smaller nonlinear behaviour due to the mass. On the contrary, the nonlinear effect due to stiffness is constant for each geometry. The damping factor has been chosen according to the experimental evidence as an average value of $\zeta\approx 2\%$; hence, equation (20) becomes:

$$m_3\ddot{w}_0^3+m_1\ddot{w}_0+c_1\dot{w}_0+k_1w_0+k_3w_0^3=f_1 \tag{25}$$

where $c_1=\zeta c_c$ for $c_c=2\sqrt{k_1m_1}$. The linear natural frequency of the PVDF plate can

be simply obtained by:

$$\omega = \sqrt{\frac{k_1}{m_1}} = \frac{4h_p}{R^2}\left(\rho S_{31}(1-\nu_p^2)\left(\frac{9}{5}+\frac{h_p^2}{R^2}\right)\right)^{-\frac{1}{2}} \tag{26}$$

whereas the critical damping takes the form:

$$c_c = \frac{8h_p^2}{9}\sqrt{\frac{\rho}{S_{31}(1-\nu_p^2)}\left(\frac{9}{5}+\frac{h_p^2}{R^2}\right)} \tag{27}$$

3.2. *Voltage output*

The radial and circumferential stresses σ_r, σ_θ for an isotropic plate with axis-symmetric displacement field are given by:

$$\begin{aligned}\sigma_r &= \frac{1}{S_{31}(1-\nu_p^2)}\left(\frac{\partial u}{\partial r}+\frac{1}{2}\left(\frac{\partial w}{\partial r}\right)^2+\nu_p\frac{u}{r}\right)\\ \sigma_\theta &= \frac{1}{S_{31}(1-\nu_p^2)}\left(\nu_p\left(\frac{\partial u}{\partial r}+\frac{1}{2}\left(\frac{\partial w}{\partial r}\right)^2\right)+\frac{u}{r}\right)\end{aligned} \tag{28}$$

By considering that the plate is polarized only along the thickness ($E_1 = E_2 = 0$), the constitutive equations of the piezoelectric plate can be written as:

$$\begin{aligned}\varepsilon_r &= S_{31}(\sigma_r - \nu_p\sigma_\theta) - d_{31}E_3\\ \varepsilon_\theta &= S_{31}(\sigma_\theta - \nu_p\sigma_r) - d_{31}E_3\\ D_3 &= -d_{31}(\sigma_r+\sigma_\theta) + \epsilon_{33}E_3\end{aligned} \tag{29}$$

where $\epsilon_{33} = \epsilon_r\epsilon_0$ is the permittivity of the piezo-electric layer and ϵ_0 is the vacuum permittivity, whereas ϵ_r is the relative permittivity.

The strain energy density is defined by:

$$U_0 = \frac{1}{2}\varepsilon_r\sigma_r + \frac{1}{2}\varepsilon_\theta\sigma_\theta + \frac{1}{2}D_3E_3 \tag{30}$$

By including the constitutive equation (29), the strain energy density becomes:

$$U_0 = \frac{1}{2}\varepsilon_r\sigma_r + \frac{1}{2}\varepsilon_\theta\sigma_\theta - \frac{1}{2}d_{31}(\sigma_r+\sigma_\theta)E_3 + \frac{1}{2}\epsilon_{33}E_3^2 \tag{31}$$

The strain energy is obtained by integrating strain energy density and including the

Table 1. Piezo-electric mechanical properties of the PVDF layer used in the simulations

	SI	Present
Density ρ	1780 kg/m^3	$1.78 \cdot 10^{-9}$ ton/mm^3
Elastic modulus E_p	2.27 GPa	2270 MPa
Poisson's ratio ν_p	0.225	
Piezo strain constant d_{31}	22 pC/N	$22 \cdot 10^{-6}$ μC/N
Relative dielectric constant ϵ_r	11	
Vacuum permittivity ϵ_0	$8.85{\cdot}10^{-12}$ F/m	8.85 nF/mm

strain and stress definitions and solutions given above as (Mo et al. (2014)):

$$\begin{aligned} U &= \int_0^R \int_0^{2\pi} \left(\int_{-h_p/2}^{h_p/2} U_0 dz \right) r d\theta dz \\ &= \frac{h_p \pi}{39690 R^2 S_{31} \left(\nu_p^2 - 1\right)} \left[(2791\nu_p^2 - 4250\nu_p - 7505) w_0^4 \right. \\ &\left. + 6615 E_3 R^2 \left(\nu_p + 1\right) \left(3R^2 E_3 \epsilon_{33} S_{31} (\nu_p - 1) + 4 d_{31} w_0^2\right) \right] \end{aligned} \tag{32}$$

The electric field is assumed to be $E_3 = V/h_p$, where V is the applied voltage. By differentiating the strain energy with respect to the voltage, the expression of the electric charge is obtained as:

$$Q = \frac{dU}{dV} = \frac{\pi \epsilon_{33} R^2}{h_p} V + \frac{2}{3} \frac{\pi d_{31}}{S_{31} \left(\nu_p - 1\right)} w_0^2 = C_{free} V + Q_{gen} \tag{33}$$

The first term is due to the external applied voltage V and the second one represents the charge generated by structural motion only ($V = 0$) Q_{gen}. Finally, the voltage generated and measured on the electrodes is obtained as:

$$V_{gen} = \frac{Q_{gen}}{C_{free}} = \frac{2}{3} \frac{h_p d_{31}}{S_{31} \epsilon_{33} R^2 (\nu_p - 1)} w_0^2 \tag{34}$$

It is remarked that the derived voltage is valid for the open-circuit condition only, and the voltage is measured only when a time-varying load p_0 is applied as in the present experimental tests.

4. Experimental data and numerical simulations

The properties of PVDF used in the simulations are listed in Table 1. The systems of units used is the most convenient to have comparable numbers in the numerical matrices. The SI units are reported for more clarity.

Three plate thicknesses are analyzed $h_p = 0.110$, 0.052, 0.028 mm and with the four different radii R considered ($R = 5$, 8, 10, 15 mm), the size to thickness ratios R/h_p range approximately between 50 and 600, which can all be studied using the classical theory of thin plates. The choice for the radius of the model referenced is due to the diameter of the most commonly used cell culture well plates (for in-vitro validation). The diameter of those wells is 35.4 mm, 22.1 mm, 16.2 mm and 11.5 mm; therefore, the

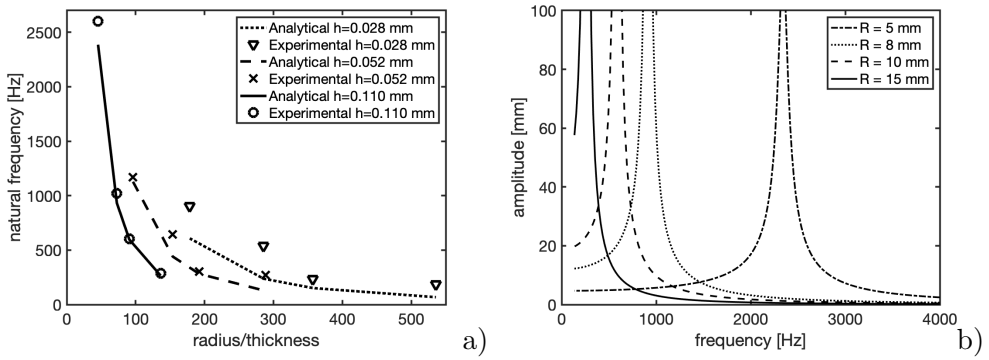

Figure 3. a) Linear natural frequencies as a function of the plate radius R. b) Harmonic response functions for each radius considering $h = 0.110$ mm.

device diameter that could best fit into these wells was chosen as 30 mm, 20 mm, 15 mm and 10 mm, accordingly. By considering the linear solution (Eq. (26)), a graphical representation of the frequency as a function of the radius is reported in Figure 3a) (recalling that $f = \omega/2\pi$, where f is the frequency and ω is angular frequency). Subsequently, the harmonic response functions that neglect nonlinear effects are depicted in figure 3b) for the plate radii investigated in the experimental tests and thickness $h = 0.110$ mm. The natural frequency of each structure is clearly identified by the linear harmonic response functions depicted and analogous functions can be represented by changing plate thickness, however, those functions are not reported for the sake of conciseness. A good match can be observed between analytical linear frequencies obtained using the present simplified approach with respect to the experimental ones, some discrepancies are noted which could be solved by considering nonlinear effects on the current geometries.

For solving the nonlinear set of equations, the well-known first-order perturbation method can be used for the case of free undamped vibrations (Wilson (2003)). This solution can be found by neglecting the nonlinear mass terms ($m_3 = 0$) and the nonlinear vibration amplitudes can be described by the following equation, in which A is the amplitude of motion of the central point of the plate and ω_0 the natural frequency of the system shown in Fig. 3b for $h = 0.110$ mm:

$$A = \sqrt{\frac{4}{3}\frac{k_1}{k_3}\left(\frac{\omega^2}{\omega_0^2} - 1\right)} \tag{35}$$

which is depicted in figure 4a) for the present structures (note that the result is independent on the plate radius). Analogously, the problem of undamped non-linear forced vibrations (induced by external oscillating stimuli) is also presented considering $m_3 = 0$ (Wilson (2003)). This solution considers that the structure vibrates as the applied load is in steady-state conditions, if the exciting force is harmonic. The solution of this problem is governed by a third-order polynomial of the form $KA^3 + (1 - \Omega^2)A - 1 = 0$, where:

$$K = \frac{3}{4}\frac{k_3}{k_1}\left(\frac{p_0}{k_1}\right)^2, \quad A = \frac{k_1}{p_0}\bar{a}, \quad \Omega = \frac{\omega}{\omega_0} \tag{36}$$

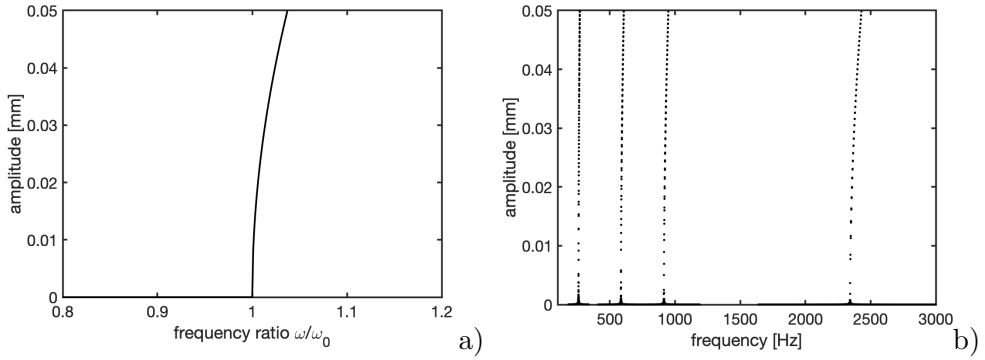

Figure 4. a)Nonlinear free vibrations. b) Nonlinear forced vibrations. By neglecting the nonlinear mass terms m_3, e.g. valid only for large plates. Radius R increases from right to left.

with $\bar{a}$ being the initial assumed displacement for the first perturbation method used in the solution. The result (presented for the plate with $h = 0.110$ mm) agrees with the free vibration case as depicted in figure 4, where the amplitude plot presents a stiffening behavior ($k_3 > 0$). Figure 4b) shows four groups of curves in which the plate radius increases from right to left, indicating that smaller plates have higher frequencies. The nonlinear term k_3 emerges for small plates and it is less relevant for large plates, where the membrane contribution becomes smaller with respect to the bending one, and the amplitude plot tends to become vertical (in other words linear). The amplitude reported in the vertical axis in Figure 4 is the term A in eq. (35). This plot recalls that in nonlinear vibrations, the natural frequency of the plates depends on plate amplitude of motion, whereas in linear vibrations the natural frequency does not depend on the amplitude.

In order to verify the nonlinear forced motion depicted in figure 4b), a numerical frequency sweep is performed by following the frequency variation shown in figure 2. Each frequency is kept constant for 2 seconds in order to let transient phenomena to be stable, retrieving the maximum plate amplitude. The results for the four geometries with $h = 0.110$ mm are represented in figure 5.

The solid lines represent the envelope of the experimental curves (obtained considering the displacement peaks in the experimental curves) shown in the supplementary material, where the displacement of the centre of each plate and the voltage output during the frequency sweep are shown in Figure 6, and the short-time Fourier transforms of the signals in relevant intervals, shown in Figure 7. The dashed curves represent the numerical data. It can be noted that the present numerical solution accurately captures the first vibration frequency for large plates ($R = 10, 15$ mm; Fig. 5c,d), whereas larger errors are observed for small plates ($R = 5, 8$ mm; Fig. 5a,b). Numerical and experimental results agree well in terms of resonance frequency, and in some cases ($R = 10, 15$ mm; Fig. 5c,d) also in terms of amplitude. The experimental resonance frequencies and those obtained from the linear and nonlinear numerical solutions are listed in table 2 for the three plate thicknesses considered. It can be observed that the relative errors obtained from the linear model are consistently larger than those predicted including nonlinear effects. The maximum relative error is smaller for thicker plates with $h = 0.110$ mm and increases for thinner plates $h = 0.028$ mm this might be due to the difficulty in the experimental side in capturing those frequencies. However, the model is able to provide rather accurate estimations of the resonance frequencies of the vibrating plates for $R = 10$, 15 and for all thicknesses.

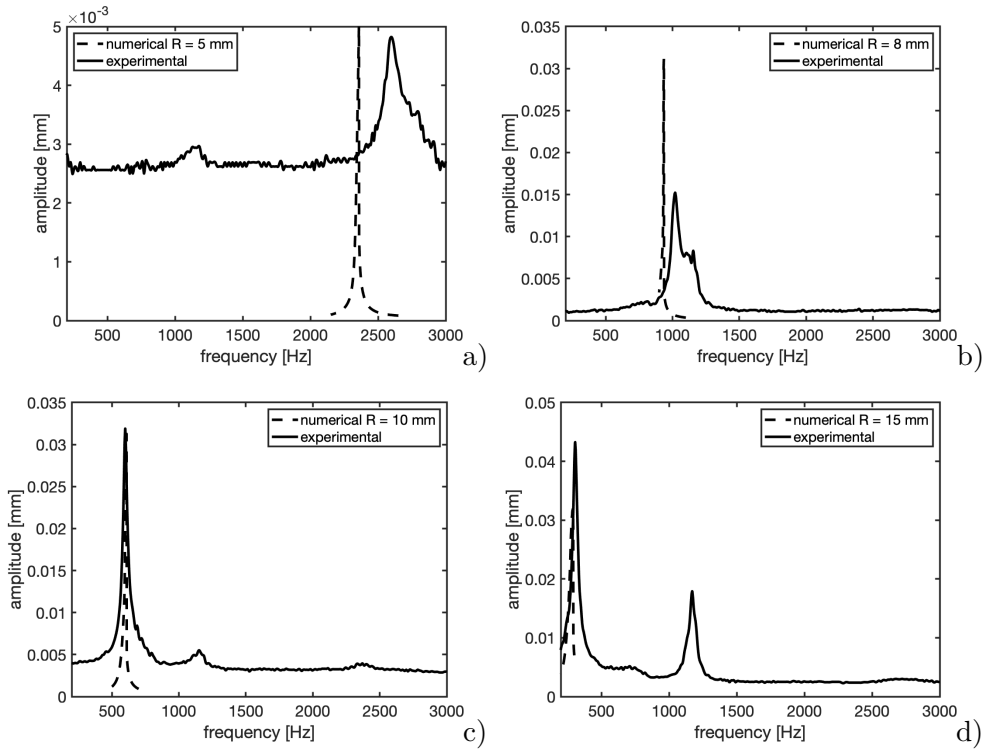

Figure 5. Frequency sweep of the nonlinear system with $m_3 = 0$ compared to the experimental results: a) $R = 5$ mm, b) $R = 8$ mm, c) $R = 10$ mm, d) $R = 15$ mm.

Table 3 shows the comparison of the voltage output obtained from the peak-to-peak values of the voltage signals at the resonance frequencies (after removing the background noise) and the absolute value of the voltage obtained from the numerical simulations. It can be noticed that the experimental values are much larger than the calculated ones. This remarkable difference can be attributed to the contribution of different factors that can affect the measured voltage. Most likely, the experimental voltage values are not only originating from the piezoelectric effect, as considered in the theory, but might reflect additional contributions, such as the triboelectric effect due to the friction between the films and the electrodes, which are dominating the electromechanical output. It is likely that during vibration, the films rub against the electrodes producing an electrical voltage through a friction-induced electrification. The extent of sliding is expected to increase with increasing the amplitude of the vibrations. However, the measured voltage might also depend on the tightness of the contact and the morphology of the surfaces in contact, which are both difficult to control. The contribution of the triboelectric effect is here confirmed by a test carried out on an unpoled extruded PVDF film (without macroscopic piezoelectric effect), which shows a non-negligible voltage (about 3 mV, after removing the background noise) output around the resonance frequency (see Fig. 8). The contribution of the piezoelectric and triboelectric effect to the voltage output has been evaluated in several types of generators and has been reported in various review papers (Xie et al. (2021); Zhang et al. (2021); Thainiramit et al. (2020) among others). The comparison of these contributions consistently indicates that the triboelectric effect usually determines a larger voltage output, which can also be orders of magnitude higher than the values only generated by the piezoelectric effect, as the present data suggest.

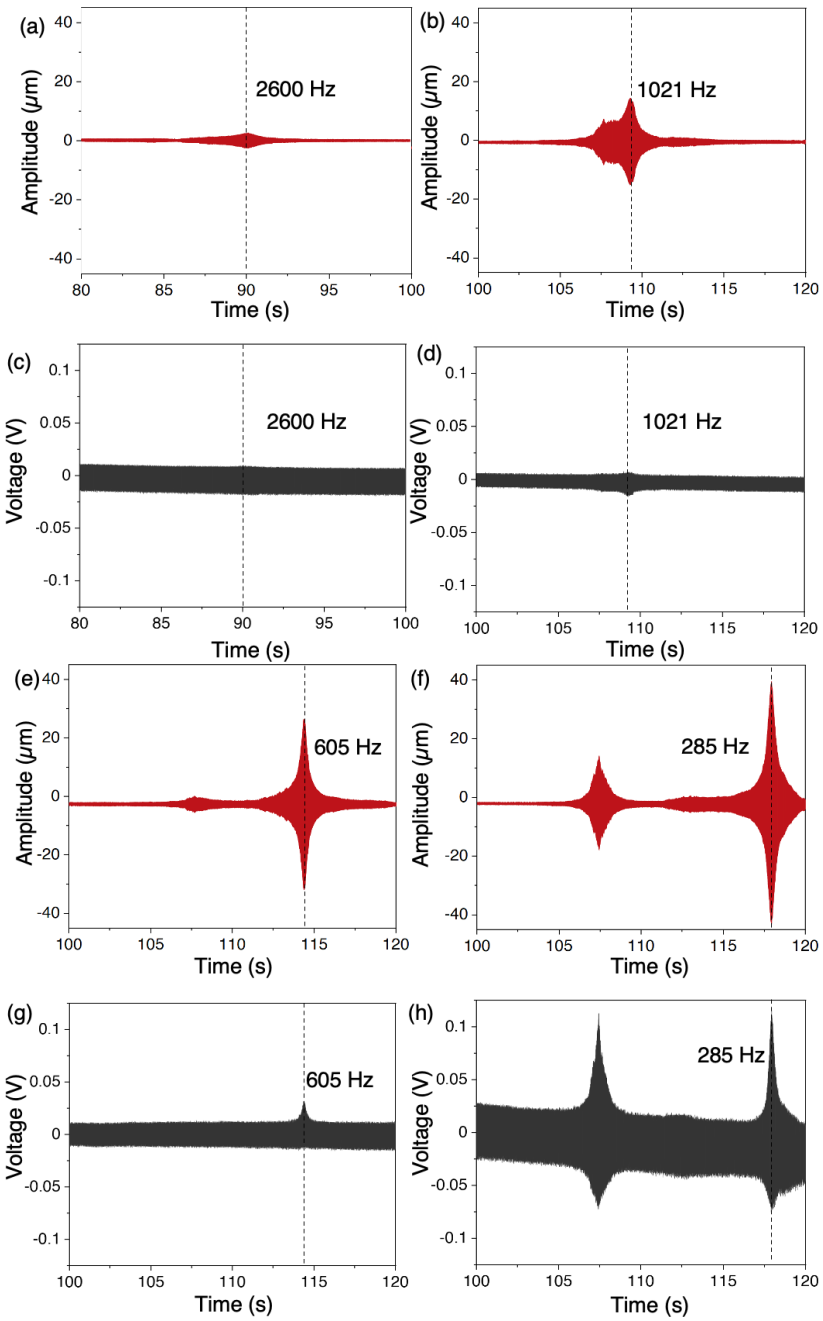

Figure 6. Displacement amplitude-time and voltage-time signals during the frequency sweep for the plates with $h = 0.110$ mm and R of a), c) $R = 5$ mm; b), d) $R = 8$ mm; e), g) $R = 10$ mm; f), h) $R = 15$ mm.

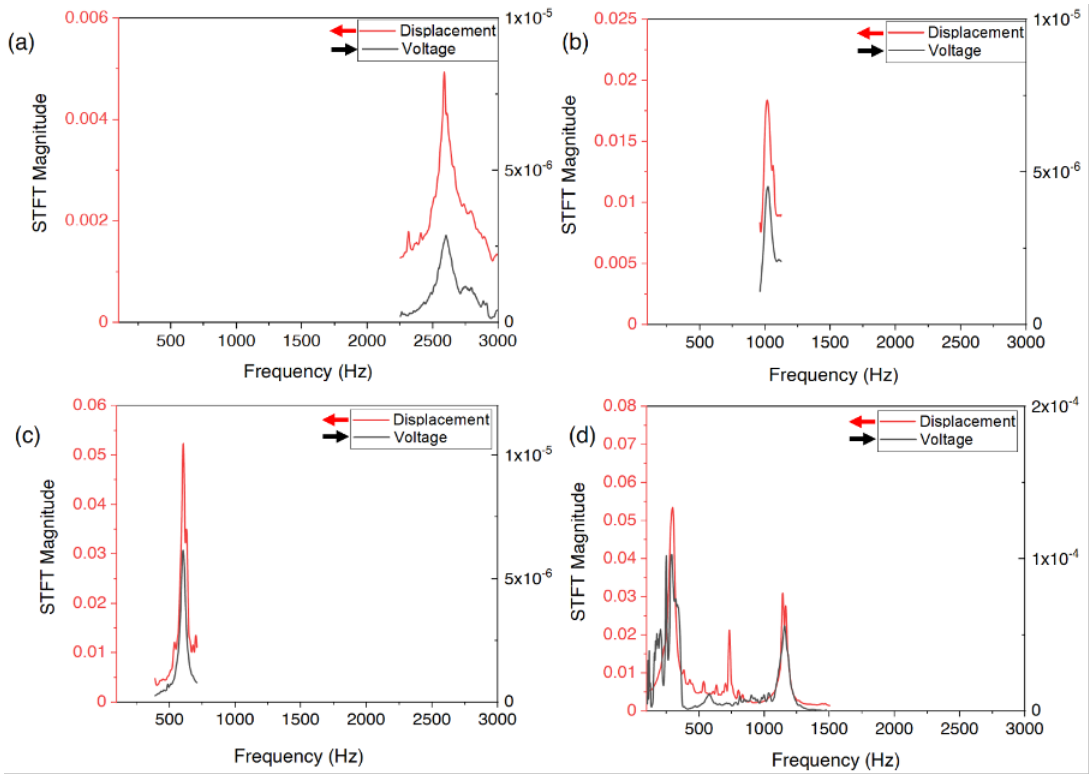

Figure 7. Short-time Fourier transforms for plates with R of a) $R = 5$ mm, b) $R = 8$ mm, c) $R = 10$ mm, d) $R = 15$ mm. Continuous lines refer to the right axis and the dashed ones to the left axis.

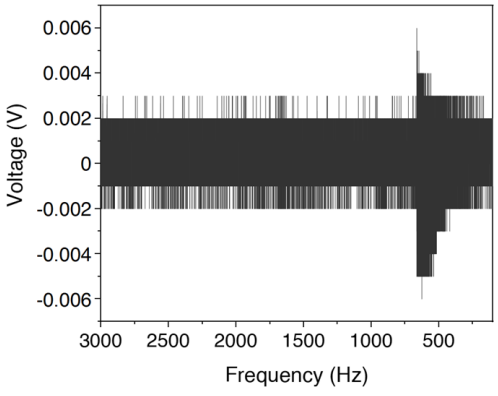

Figure 8. Voltage-frequency signal of an unpoled PVDF film of $R = 15$ mm collected under SPL level of 112 dB on average.

Table 2. Linear and nonlinear natural frequencies [Hz] for the four radii considered (relative error in brackets).

radius R [mm]	5	8	10	15
$h = 0.110$ mm				
experimental	2602	1021	605	285
linear	2386.52	932.23	596.63	265.17
	(8.28%)	(8.69%)	(1.38%)	(6.96%)
nonlinear	2386.55	933.00	602.07	285.57
	(8.28%)	(8.62%)	(0.48%)	(0.31%)
$h = 0.052$ mm				
experimental	1170	645	304	270
linear	1128.17	440.69	282.04	125.35
	(3.58%)	(31.68%)	(7.22%)	(53.57%)
nonlinear	1128.58	447.15	304.05	281.81
	(3.54%)	(30.67%)	(0.02%)	(4.37%)
$h = 0.028$ mm				
experimental	906	541	236	186
linear	607.48	237.30	151.87	67.50
	(32.95%)	(53.141%)	(35.65%)	(63.71%)
nonlinear	612.18	295.84	205.7524	143.112
	(32.43%)	(45.32%)	(12.82%)	(23.06%)

Table 3. Comparison of voltage output [mV] values obtained from the experiments at the resonance frequency and from the simulations for the plates of different diameter.

radius R [mm]	5	8	10	15
$h = 0.110$ mm				
experimental	4	12	22	128
numerical	0.0146	0.068	0.364	0.196
$h = 0.052$ mm				
numerical	0.1103	0.0673	0.0844	0.3063
$h = 0.028$ mm				
numerical	0.3006	0.1449	0.1122	0.1649

An additional possible contribution to the voltage output might come from the flexoelectric effect, consisting of the generation of electric charges separation (polarization) induced by a local strain gradient. In these particular vibrating conditions, the films are under bending; therefore, there will be a strain gradient along the thickness of the films that can contribute to the voltage output. It is possible that this effect is amplified in resonance conditions. The verification of this hypothesis lies outside the scope of the present work and will be considered in a separate and more detailed study.

5. Conclusions

The present manuscript reports a detailed study on the vibrations of PVDF piezoelectric thin films induced by acoustic sound with frequency in the range of 100 Hz-10 kHz based on experimental tests and a theoretical model. The measurements were carried out on disks of different diameters using a laser vibrometer and have enabled the identification of the resonance frequencies, which decrease with increasing the di-

ameter of the disks, as expected. The theoretical model is based on the classical thin plate theory and has been developed using Kirchoff's assumptions in axis-symmetric conditions to predict the vibration amplitudes and resonance frequencies of the disks. The derived equation of motion includes a small damping and nonlinear effects related to mass and stiffness, and it has been solved using the first-order perturbation method, providing accurate predictions of the resonance behaviour. The linear model determines an error slightly higher than 10% in the prediction of the experimental resonance frequencies, while the nonlinear model leads to lower errors. The estimation of the voltage output originating from the piezoelectric properties of the films obtained from the model is much lower than the experimental values, indicating that additional effects are affecting the voltage measured. The discrepancy has been mainly attributed to the electrification caused by the friction of the films against the electrodes occurring during vibration and an eventual contribution of the flexoelectric effect possibly enhanced in resonance conditions.

References

Ahamed, R., Choi, S.-B., and Ferdaus, M. M. (2018). A state of art on magneto-rheological materials and their potential applications. *Journal of Intelligent Material Systems and Structures*, 29(10):2051–2095.

Ali, W. R. and Prasad, M. (2020). Piezoelectric mems based acoustic sensors: A review. *Sensors and Actuators A: Physical*, 301:111756.

Baratchi, M., Meratnia, N., Havinga, P. J. M., Skidmore, A. K., and Toxopeus, B. A. G. (2013). Sensing solutions for collecting spatio-temporal data for wildlife monitoring applications: A review. *Sensors*, 13(5):6054–6088.

Basaeri, H., Christensen, D. B., and Roundy, S. (2016). A review of acoustic power transfer for bio-medical implants. *Smart Materials and Structures*, 25(12):123001.

Benech, P. and Duchamp, J. (2016). Piezoelectric materials in rf applications. In Ogawa, T., editor, *Piezoelectric Materials*, chapter 9, pages 266–290. IntechOpen.

Caliò, R., Rongala, U. B., Camboni, D., Milazzo, M., Stefanini, C., De Petris, G., and Oddo, C. M. (2014). Piezoelectric energy harvesting solutions. *Sensors*, 14(3):4755–4790.

Carrera, E., Brischetto, S., and Nali, P. (2008). Variational statements and computational models for multifield problems and multilayered structures. *Mechanics of Advanced Materials and Structures*, 15(3-4):182–198.

Chanda, A. G. and Sahoo, R. (2021). Finite element analysis of smart composite plate structures coupled with piezoelectric materials: Investigation of static and vibration responses. *Mechanics of Advanced Materials and Structures*, 0(0):1–26.

Chen, D., Chen, K., Brown, K., Hang, A., and Zhang, J. X. J. (2017). Liquid-phase tuning of porous pvdf-trfe film on flexible substrate for energy harvesting. *Applied Physics Letters*, 110(15):153902.

Choi, J., Jung, I., and Kang, C.-Y. (2019). A brief review of sound energy harvesting. *Nano Energy*, 56:169 – 183.

Cinefra, M., Carrera, E., and Valvano, S. (2015a). Variable kinematic shell elements for the analysis of electro-mechanical problems. *Mechanics of Advanced Materials and Structures*, 22(1-2):77–106.

Cinefra, M., Lamberti, A., Zenkour, A. M., and Carrera, E. (2015b). Axiomatic/asymptotic technique applied to refined theories for piezoelectric plates. *Mechanics of Advanced Materials and Structures*, 22(1-2):107–124.

Drafts, B. (2001). Acoustic wave technology sensors. *IEEE Transactions on Microwave Theory and Techniques*, 49(4):795–802.

Duan, W., Quek, S., and Wang, Q. (2005). Free vibration analysis of piezoelectric coupled thin and thick annular plate. *Journal of Sound and Vibration*, 281(1):119–139.

Eisenmenger, W. and Haardt, M. (1982). Observation of charge compensated polarization zones in polyvinylindenfluoride (pvdf) films by piezoelectric acoustic step-wave response. *Solid State Communications*, 41(12):917–920.

Erturk, A. and Inman, D. (2011). *Piezoelectric Energy Harvesting*. Wiley.

Fu, Y., Luo, J., Nguyen, N., Walton, A., Flewitt, A., Zu, X., Li, Y., McHale, G., Matthews, A., Iborra, E., Du, H., and Milne, W. (2017). Advances in piezoelectric thin films for acoustic biosensors, acoustofluidics and lab-on-chip applications. *Progress in Materials Science*, 89:31–91.

Gualtieri, J., Kosinski, J., and Ballato, A. (1994). Piezoelectric materials for acoustic wave applications. *IEEE Transactions on Ultrasonics, Ferroelectrics, and Frequency Control*, 41(1):53–59.

Hashimoto, K.-y. (2011). Demands of highly piezoelectric materials for radio frequency acoustic wave devices. *physica status solidi (a)*, 208(5):1084–1092.

Hosseini-Hashemi, S., Azimzadeh-Monfared, M., and Rokni Damavandi Taher, H. (2010). A 3-d ritz solution for free vibration of circular/annular functionally graded plates integrated with piezoelectric layers. *International Journal of Engineering Science*, 48(12):1971–1984.

Hosseini Hashemi, S., Es'haghi, M., and Karimi, M. (2010). Closed-form vibration analysis of thick annular functionally graded plates with integrated piezoelectric layers. *International Journal of Mechanical Sciences*, 52(3):410–428.

Inaoka, T., Shintaku, H., Nakagawa, T., Kawano, S., Ogita, H., Sakamoto, T., Hamanishi, S., Wada, H., and Ito, J. (2011). Piezoelectric materials mimic the function of the cochlear sensory epithelium. *Proceedings of the National Academy of Sciences*, 108(45):18390–18395.

Jain, A., Kumar, S. J., Kumar, M. R., Ganesh, A. S., and Srikanth, S. (2014). Pvdf-pzt composite films for transducer applications. *Mechanics of Advanced Materials and Structures*, 21(3):181–186.

Kim, H., Kim, J.-H., and Kim, J. (2011). A review of piezoelectric energy harvesting based on vibration. *International Journal of Precision Engineering and Manufacturing*, 12:1129–1141.

Kim, Y., Kang, J., Kim, D., Kim, E., Chong, P., and Seo, S. (2008). Design of a fence surveillance system based on wireless sensor networks. In *Proceedings of the 2nd International Conference on Autonomic Computing and Communication Systems, Autonomics 2008, September 23-25, 2008, Turin, Italy*, page 4.

Kong, F., Chang, M., and Wang, Z. (2021). Analysis of fracture damage and friction mechanical properties of silicon dioxide/polyvinylidene composites. *Mechanics of Advanced Materials and Structures*, 0(0):1–11.

Lang, C., Fang, J., Shao, H., Ding, X., and Lin, T. (2016). High-sensitivity acoustic sensors from nanofibre webs. *Nature communications*, 7:11108.

Lee, H. S., Chung, J., Hwang, G.-T., Jeong, C. K., Jung, Y., Kwak, J.-H., Kang, H., Byun, M., Kim, W. D., Hur, S., Oh, S.-H., and Lee, K. J. (2014). Flexible inorganic piezoelectric acoustic nanosensors for biomimetic artificial hair cells. *Advanced Functional Materials*, 24(44):6914–6921.

Liu, B., Jiang, Q., Hu, Y., and Yang, J. (2011). High-frequency vibrations of piezoelectric plates driven by lateral electric fields. *International Journal of Engineering Science*, 49(12):1435–1442. Advances in generalized continuum mechanics.

Liu, H., Zhong, J., Lee, C., Lee, S.-W., and Lin, L. (2018). A comprehensive review on piezoelectric energy harvesting technology: Materials, mechanisms, and applications. *Applied Physics Reviews*, 5(4):041306.

M. Ericka, D. Vasic, F. Costa, G. Poulin, and S. Tliba (2005). Energy harvesting from vibration using a piezoelectric membrane. *J. Phys. IV France*, 128:187–193.

Mahidhar, R., Prakash, K., Aswathi, R. N., Prasad, M. V. N., and Sambandan, S. (2013). Vibration spectrum analyzer using stretched membranes of polymer piezoelectrics for sensor networks. *Measurement Science and Technology*, 24(5):055108.

Mankin, R. W., Hagstrum, D. W., Smith, M. T., Roda, A. L., and Kairo, M. T. K. (2011). Perspective and Promise: a Century of Insect Acoustic Detection and Monitoring. *American*

Entomologist, 57(1):30–44.

Mo, C., Davidson, J., and Clark, W. W. (2014). Energy harvesting with piezoelectric circular membrane under pressure loading. *Smart Materials and Structures*, 23:045005.

Paul, H. and Natarajan, K. (1994). Flexural vibration in a finite piezoelectric circular cylinder of crystal class 6 mm. *International Journal of Engineering Science*, 32(8):1303–1314.

Pillai, M. A. and Deenadayalan, E. (2014). A review of acoustic energy harvesting. *International Journal of Precision Engineering and Manufacturing*, 15(5):949–965.

Proctor, T. M. (1982). An improved piezoelectric acoustic emission transducer. *The Journal of the Acoustical Society of America*, 71(5):1163–1168.

Roes, M. G. L., Duarte, J. L., Hendrix, M. A. M., and Lomonova, E. A. (2013). Acoustic energy transfer: A review. *IEEE Transactions on Industrial Electronics*, 60(1):242–248.

Safari, A. and Akdogan, E. (2008). *Piezoelectric and Acoustic Materials for Transducer Applications*. Springer US.

Sanz-Robinson, J., Huang, L., Moy, T., Rieutort-Louis, W., Hu, Y., Wagner, S., Sturm, J. C., and Verma, N. (2016). Large-area microphone array for audio source separation based on a hybrid architecture exploiting thin-film electronics and cmos. *IEEE Journal of Solid-State Circuits*, 51(4):979–991.

Shin, Y.-H., Jung, I., Park, H., Pyeon, J. J., Son, J. G., Koo, C. M., Kim, S., and Kang, C.-Y. (2018). Mechanical fatigue resistance of piezoelectric pvdf polymers. *Micromachines*, 9(10).

Shintaku, H., Nakagawa, T., Kitagawa, D., Tanujaya, H., Kawano, S., and Ito, J. (2010). Development of piezoelectric acoustic sensor with frequency selectivity for artificial cochlea. *Sensors and Actuators A: Physical*, 158(2):183 – 192.

Thainiramit, P., Yingyong, P., and Isarakorn, D. (2020). Impact-driven energy harvesting: Piezoelectric versus triboelectric energy harvesters. *Sensors*, 20(20).

Tiersten, H. (2013). *Linear Piezoelectric Plate Vibrations: Elements of the Linear Theory of Piezoelectricity and the Vibrations Piezoelectric Plates*. Springer US.

Tocci Monaco, G., Fantuzzi, N., Fabbrocino, F., and Luciano, R. (2021a). Critical temperatures for vibrations and buckling of magneto-electro-elastic nonlocal strain gradient plates. *Nanomaterials*, 11(1).

Tocci Monaco, G., Fantuzzi, N., Fabbrocino, F., and Luciano, R. (2021b). Trigonometric solution for the bending analysis of magneto-electro-elastic strain gradient nonlocal nanoplates in hygro-thermal environment. *Mathematics*, 9(5).

Toprak, A. and Tigli, O. (2014). Piezoelectric energy harvesting: State-of-the-art and challenges. *Applied Physics Reviews*, 1(3):031104.

Vieira, F. S. and Araújo, A. L. (2021). Implicit non-ordinary state-based peridynamics model for linear piezoelectricity. *Mechanics of Advanced Materials and Structures*, 0(0):1–22.

Viola, G., Chang, J., Maltby, T., Steckler, F., Jomaa, M., Sun, J., Edusei, J., Zhang, D., Vilches, A., Gao, S., Liu, X., Saeed, S., Zabalawi, H., Gale, J., and Song, W. (2020). Bioinspired multiresonant acoustic devices based on electrospun piezoelectric polymeric nanofibers. *ACS applied materials & interfaces*, 12(31):34643–34657.

Wang, Y.-T., Hu, Y.-C., and Chen, K.-R. (2015). A flexible polyvinylidene fluoride film-loudspeaker. *Journal of the Chinese Society of Mechanical Engineers, Transactions of the Chinese Institute of Engineers - Series C*, 36:219–251.

Wilson, J. (2003). *Dynamics of Offshore Structures*. Wiley.

Xie, L., Zhai, N., Liu, Y., Wen, Z., and Sun, X. (2021). Hybrid triboelectric nanogenerators: From energy complementation to integration. *Research*, 2021:9143762.

Yadav, D., Yadav, J., Vashistha, R., Goyal, D. P., and Chhabra, D. (2021). Modeling and simulation of an open channel pehf system for efficient pvdf energy harvesting. *Mechanics of Advanced Materials and Structures*, 28(8):812–826.

Zhang, J., He, Y., Boyer, C., Kalantar-Zadeh, K., Peng, S., Chu, D., and Wang, C. H. (2021). Recent developments of hybrid piezo–triboelectric nanogenerators for flexible sensors and energy harvesters. *Nanoscale Adv.*, 3:5465–5486.

Zhang, Z., Feng, C., and Liew, K. (2006). Three-dimensional vibration analysis of multilayered piezoelectric composite plates. *International Journal of Engineering Science*, 44(7):397–408.

Zhao, Z., Wang, B., Qian, Z., and Yong, Y.-K. (2020). A novel approach to quantitative predictions of high-frequency coupled vibrations in layered piezoelectric plates. *International Journal of Engineering Science*, 157:103407.

Zhou, P. (2021). On the coupling effects between elastic and electromagnetic fields from the perspective of conservation of energy.